Supplementary Figures

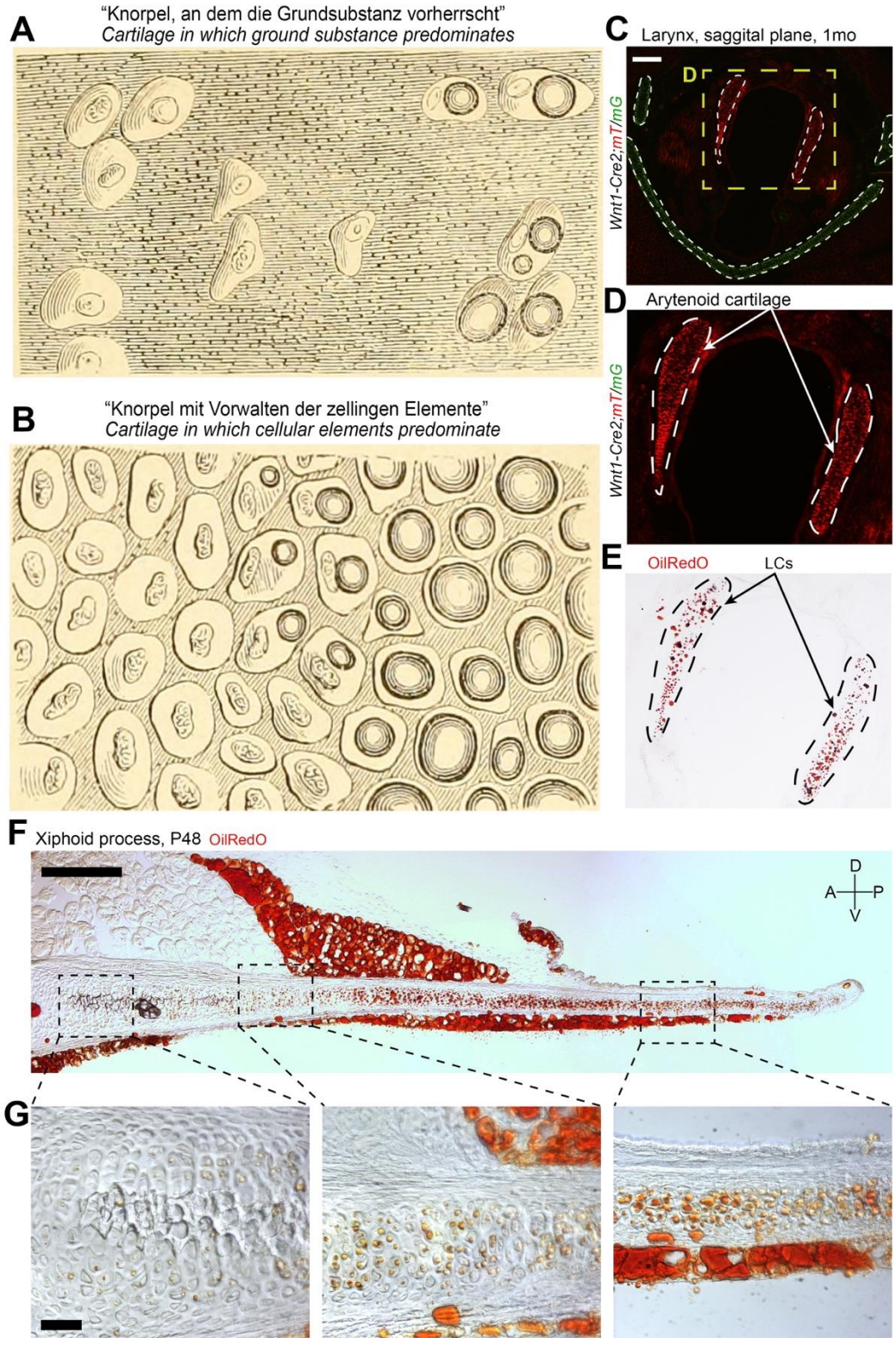

Fig. S1: Lipocartilages in rodents. (**A, B**) First recorded observations on lipocartilage by Franz Leydig. Depiction of the portion of rat ear cartilage, in which individual lacunae are encased in large amounts of extracellular matrix (**A**). Depiction of the portion of rat ear cartilage, in which chondrocytes, rather than extracellular matrix, are the predominant element of the tissue (**B**). In both panels, Leydig represents cytoplasmic lipid vacuoles as concentric circles, which in some cells on (**B**; right side) occupy the majority of the intracellular space. (**C-D**) Transverse sections of larynx from *Wnt1-Cre2;mT/mG* mice reveal that it contains cartilage elements of distinct embryonic origin, including neural crest-derived thyroid cartilage (GFP^+) and non-neural crest-derived arytenoid cartilages (RFP^+). (**E**) OilRedO staining reveals that both thyroid and arytenoid cartilages in mice contain lipid-laden lipochondrocytes. (**F-G**) Cross-section of the sternum xiphoid process in a P48 mouse following OilRedO staining. The xiphoid shows as a cartilage plate (**F**) comprised of chondrocytes with distinct degrees of lipid accumulation, with lipochondrocytes preferentially forming towards the posterior tip (distal) of the process. LCs, lipochondrocytes. Scale bars: (C), 500 μm; (F), 200 μm. (A) and (B) are reproduced with modifications from Leydig F., 1857 (not in copyright).

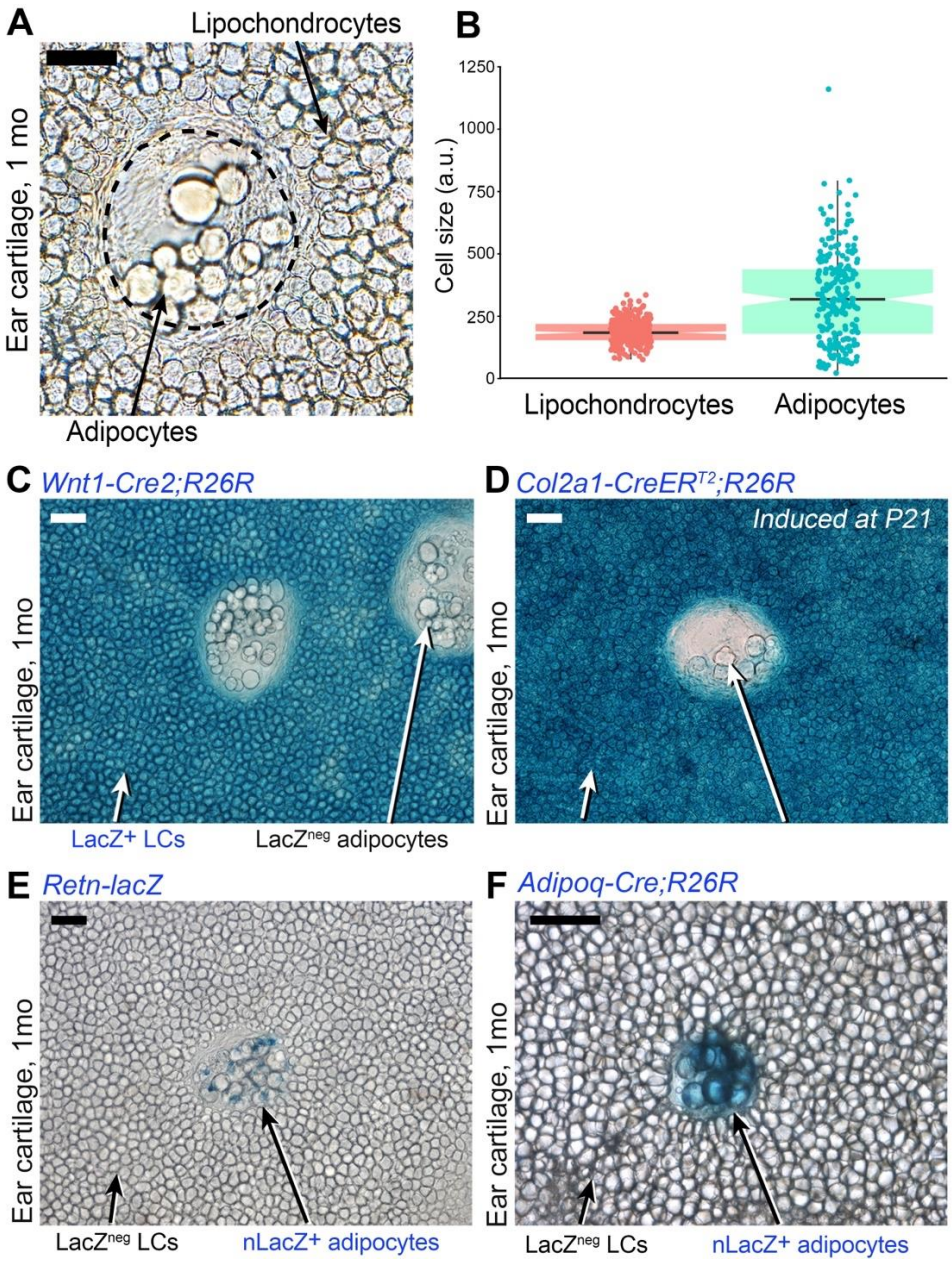

Fig. S2: Morphological and lineage analyses of mouse ear lipochondrocytes. (**A-B**) Lipochondrocytes and fenestrae-bound adipocytes significantly differ in size. (**A**) Lipochondrocytes and adjacent adipocytes within ear lipo-cartilage fenestrae have similar morphologies in one-month-old mice. (**B**) Despite their similar appearance, the range of lipochondrocyte sizes is consistently uniform throughout the ear lipocartilage plate (red) compared to the broadly varying size distribution of adipocytes in fenestrae (teal). (**C-F**) Ear lipochondrocytes are lacZ-positive in *Wnt1-Cre2;R26R* (**C**) and *Col2a1-CreER^{T};R26R* mice (**D**), but negative in adipocyte-specific *Retn-lacZ* (**E**) and *Adipoq-Cre;R26R* mice (**F**). Scale bars: (A), 50 μm; (C-E), 100 μm.

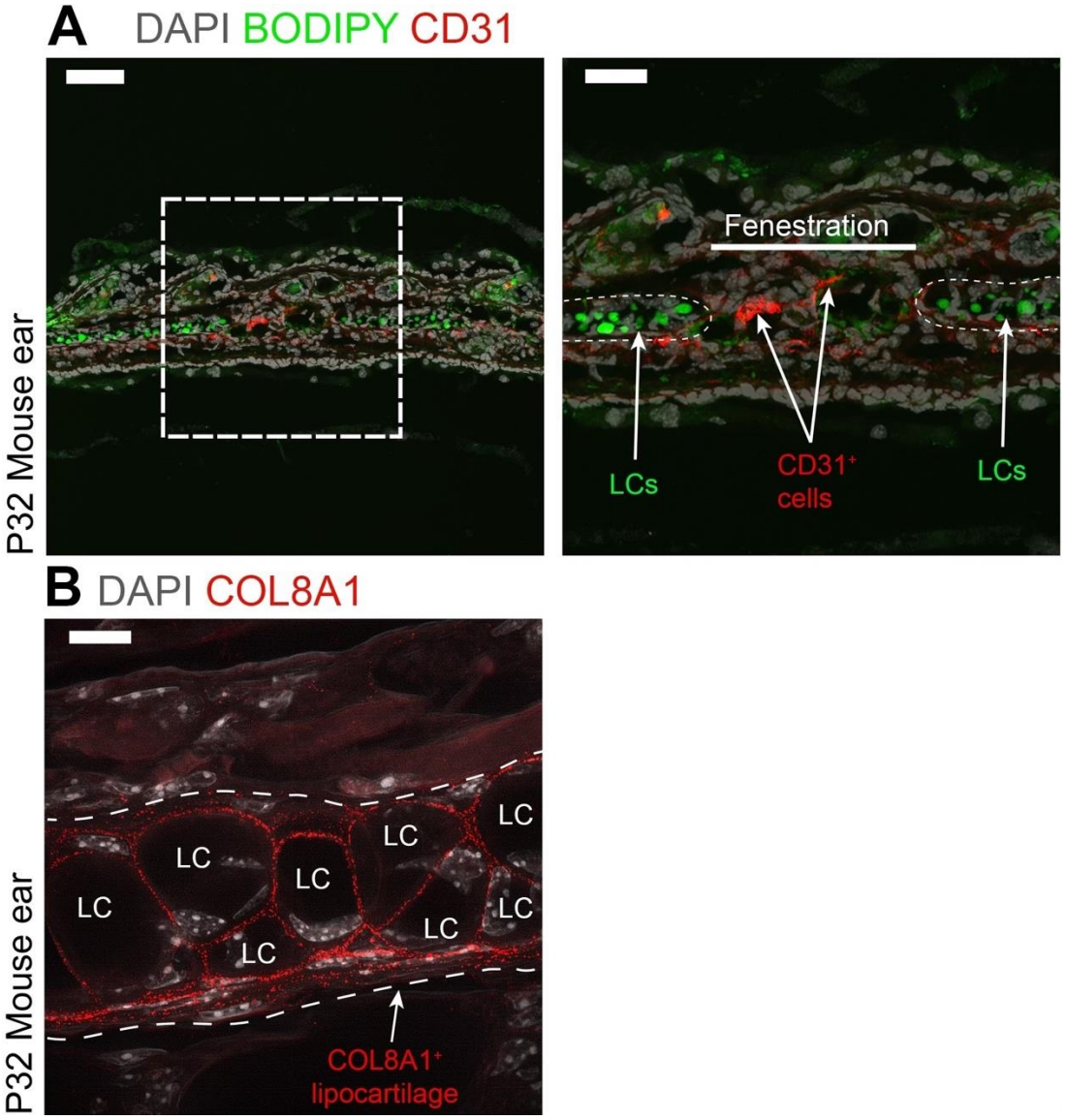

Fig. S3: Immunostaining analysis on mouse ear lipocartilage and fenestra-resident cells. (**A**) Lipid staining (BODIPY) and anti-CD31 immunostaining on adult mouse ear reveals that $CD31^+$ endothelial cells occupy fenestrae within $BODIPY^+$ lipocartilage, suggesting that fenestrae serve as openings for traversing blood vessels. (**B**) Super-resolution imaging of anti-COL8A1 immunostaining on adult ear lipocartilage shows localization of COL8A1 along individual LC boundaries and perichondrium. Scale bars: (A, left), 100 µm; (A, right), 50 µm; (B), 10 µm.

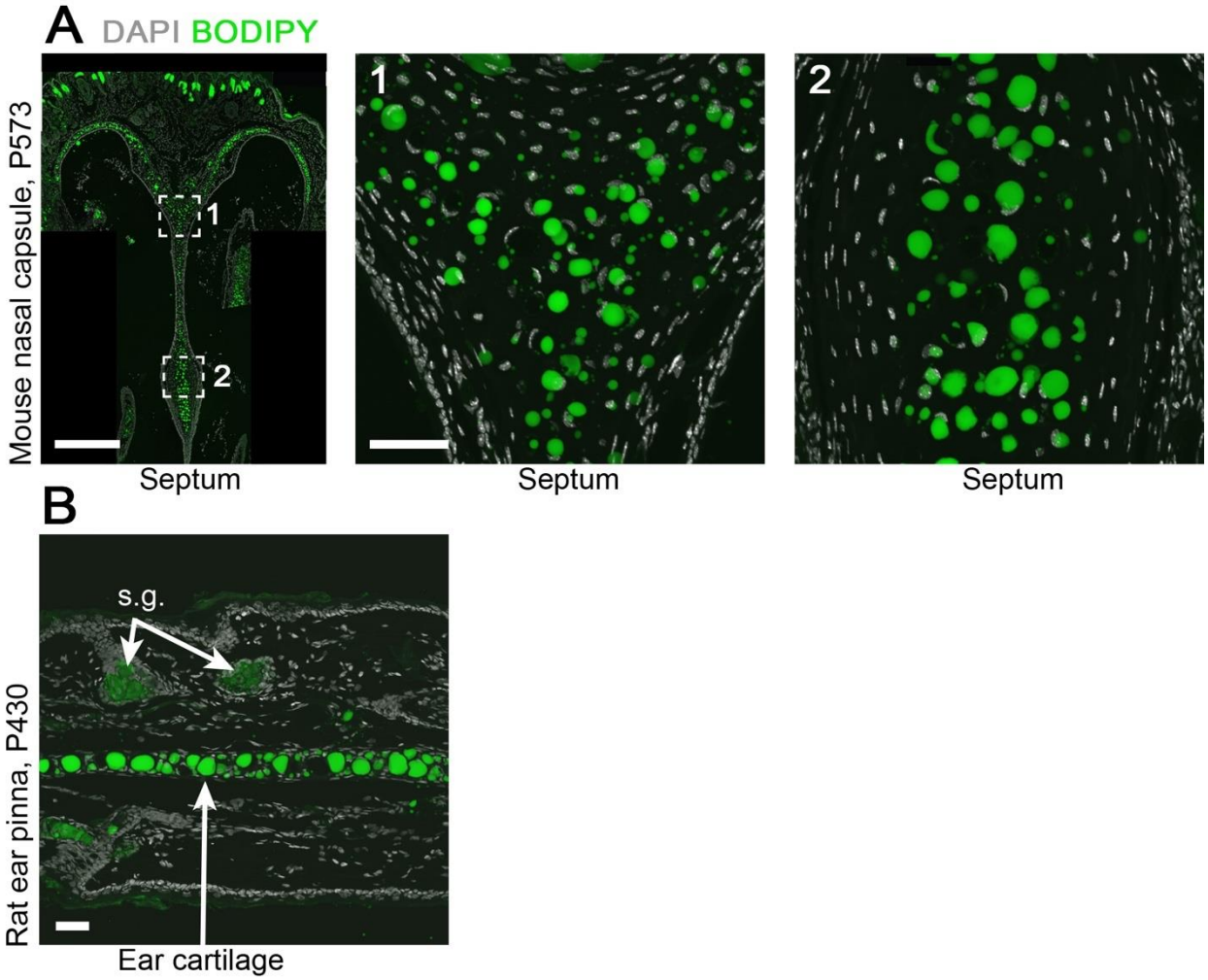

Fig. S4: Lipid staining of cranial cartilages in aged animals. (**A**) BODIPY staining (green) of mouse nasal capsule at P573 shows lipid vacuoles-containing cells (lipochondrocytes) across the nasal cartilage. Left—composite image. Center and right—magnified views of the insets 1 and 2, showing large lipid vacuoles in cells of the distal (center) and proximal (right) nasal lipocartilage septum. (**B**) In P430 rat, BODIPY staining (green) shows lipid vacuoles-containing lipochondrocytes in the ear lipocartilage. Adjacent sebaceous glands (s.g.) are annotated for clarity. Scale bars: (A, left), 500 µm; (A, center; B), 50 µm.

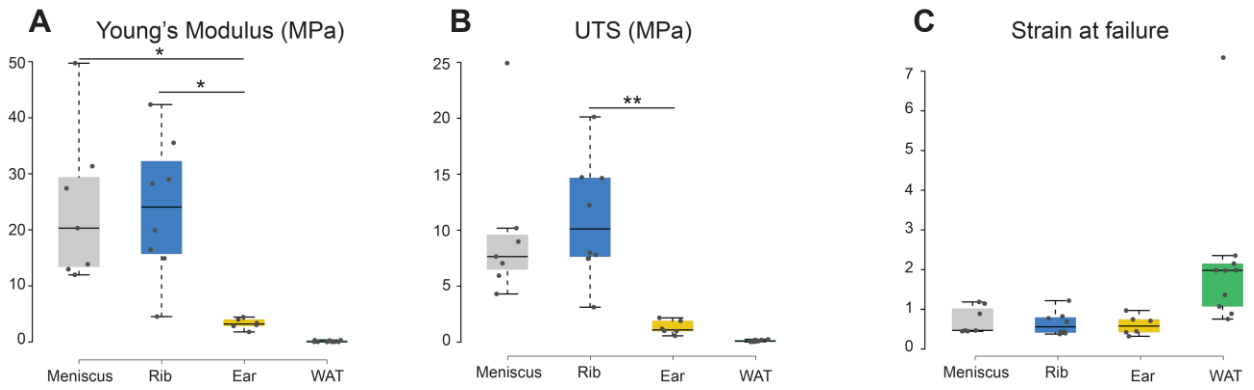

Fig. S5: Comparative biomechanical properties of mouse cartilages and adipose tissue. Uniaxial biomechanical testing under tension of knee meniscus (Meniscus; gray), rib cartilage (Rib; blue), ear lipocartilage (Ear; yellow), and inguinal white adipose tissue (WAT; green). Compared to lipocartilage, knee meniscus and rib cartilages show significantly higher values for (**A**) Young's modulus (23.94±5.14 and 23.86±4.32 MPa, respectively; Welch's ANOVA with Dunnett's T3 multiple comparison tests, p=0.0338 and p=0.0108, respectively) and (**B**) ultimate tensile strength (9.86±2.61 and 11.01±1.91 MPa, respectively; Welch's ANOVA with Dunnett's T3 multiple comparison tests, p=0.0799 and p=0.0079, respectively). (**C**) Since Welch's ANOVA showed no significance for strain at failure values (0.72±0.12 for knee meniscus, 0.64±0.10 for rib cartilage, 0.60±0.09 for lipocartilage, and 2.19±1.89 for adipose tissue), a *post hoc* test was not performed. Note that values shown for Ear and WAT are identical to these shown in main Fig. 1M.

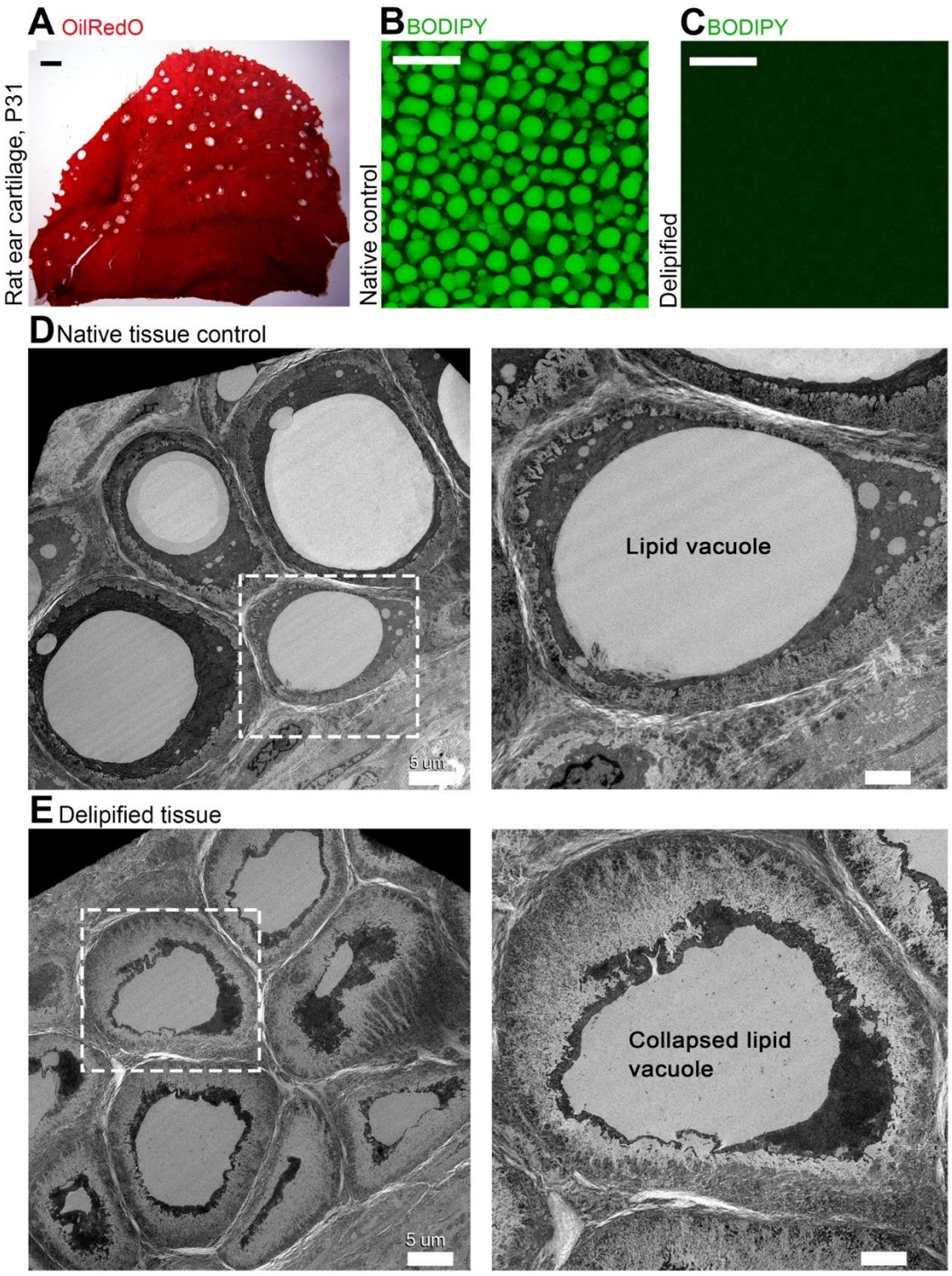

Fig. S6: Confirmation of effective delipification of rat ear lipocartilage. (**A**) Micro-dissected rat ear lipocartilage following OilRedO staining. (**B-E**) Lipid droplet analysis in freshly dissected (**B, D**) or delipified lipocartilage (**C, E**) following BODIPY staining (**B, C**) or transmission electron microscopy (**D, E**). Both assays show prominent loss of lipid droplets following delipification. Scale bars: (A), 1mm; (B, C), 100 µm; (D, E, left), 5 µm; (D, E, right), 2 µm.

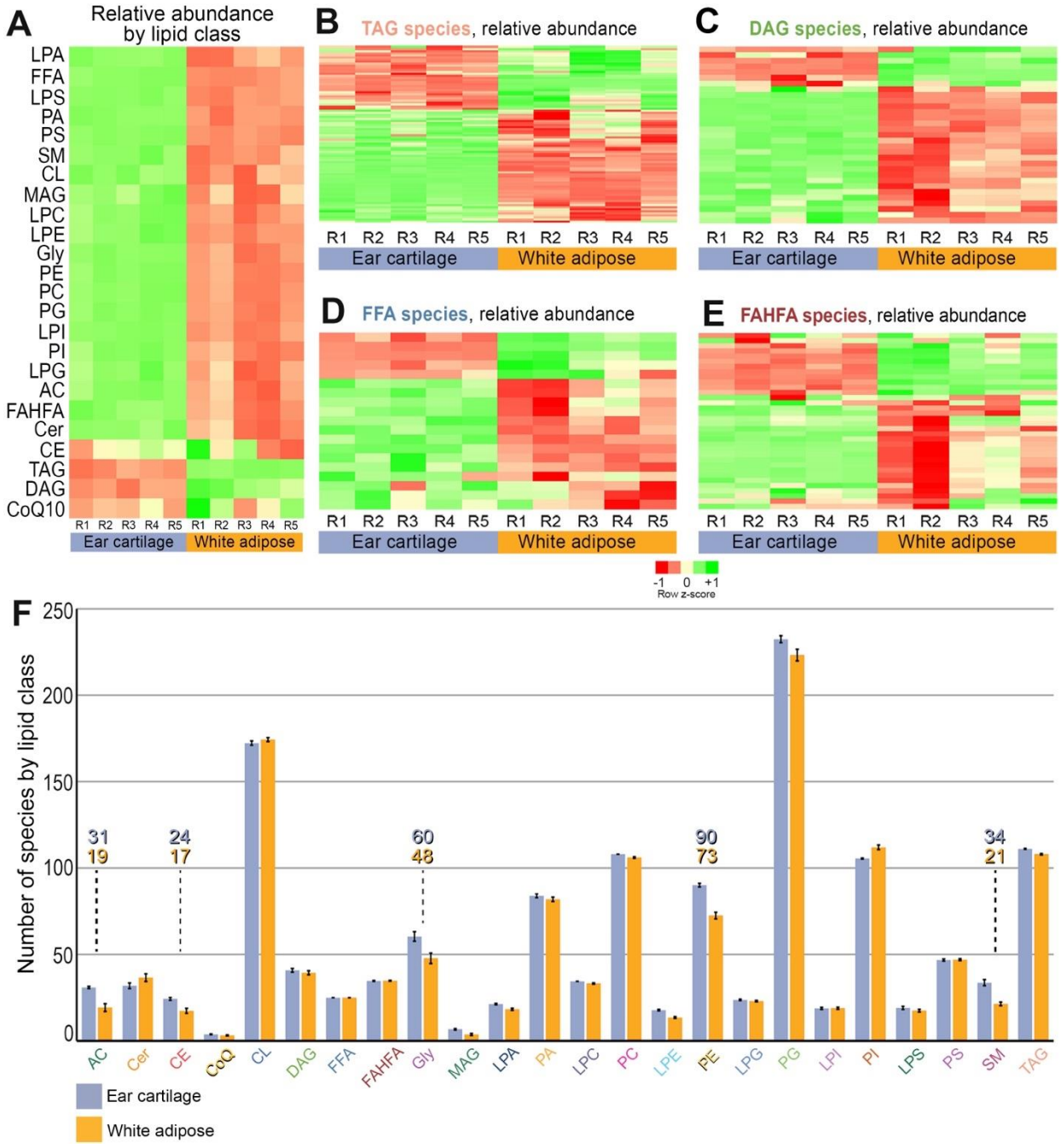
A
Relative abundance by lipid class
LPA
FFA
LPS
PA
PS
SM
CL
MAG
LPC
LPE
Gly
PE
PC
PG
LPI
PI
LPG
AC
FAHFA
Cer
CE
TAG
DAG
CoQ10
R1 R2 R3 R4 R5 R1 R2 R3 R4 R5
Ear cartilage
White adipose
B
TAG species, relative abundance
C
DAG species, relative abundance
D
FFA species, relative abundance
E
FAHFA species, relative abundance
-1 0 +1
Row z-score
F
Number of species by lipid class
250
200
150
100
50
0
31
19
24
17
60
48
90
73
34
21
AC Cer CE CoQ CL DAG FFA FAHFA Gly MAG LPA PA LPC PC LPE PE LPG PG LPI PI LPS PS SM TAG
Ear cartilage
White adipose

Fig. S7: Lipidomic profile of ear lipocartilage is distinct from that of white adipose tissue. (**A-E**) Heatmaps show that within the detected neutral lipid classes, ear lipo-cartilage and inguinal white adipose tissue are enriched for distinct molecular species. The definition of heatmap colors follows that of main Fig. 2A. (**F**) Bar chart shows that in comparison with white adipose tissue (yellow), lipocartilage (blue) has more diverse lipid composition (i.e., more detected molecular species), especially within the classes of acyl carnitines (AC), cholesteryl esters (CE), glycolipids (Gly), phosphatidylethanolamines (PE) and sphingomyelins (SM). See Table S1 for the definition of all lipid classes. This lipidomic analysis reveals lipid species abundance and diversity in lipochondrocytes. Neutral lipids, the primary molecular species of lipid vacuoles, constitute the majority of the tissue's lipids both in the ear cartilage and WAT; yet, their relative abundance is distinct. The WAT lipidome is dominated by triglycerides (86.5+/-12.36%), followed by fatty acid hydroxyl-fatty acids (FAHFAs; 9.4+/-2.5%) and diglycerides (1.7+/-0.001%). Notably, triglycerides constitute only 43.3+/-0.78% of cartilage lipids, half of that of WAT, while FAHFAs make a considerably larger contribution, at 31.1+/-3.1%. The low relative abundance of triglycerides in ear cartilage indicates that their synthesis, utilization, or both are suppressed. Consistent with the latter possibility, several molecular classes that are precursors in triglyceride synthesis, namely free fatty acids (FFAs) (7.6+/-0.2% *vs.* 0.9+/-0.1%), lysophosphatidic acids (1.2+/-0.2% *vs.* 0.04+/-0.007%) and phosphatidic acids (5.0+/-0.4% *vs.* 0.5+/-0.05%), preferentially accumulate in ear cartilage compared to WAT. In addition to overall abundance differences between ear cartilage and WAT, neutral lipids show distinct relative abundance profiles within each class (**B-E**), suggesting differences in their biogenesis. Beyond neutral lipids, the ear cartilage lipidome differs from that of WAT across several other lipid classes. Ear cartilage has a more diverse composition of glycolipids (60 species in cartilage *vs.* 48 in WAT), phosphatidylethanolamines, a class of phospholipids (90 *vs.* 73), sphingomyelins (34 *vs.* 21), cholesteryl esters (24 *vs.* 17) and acyl carnitines (31 *vs.* 19) (**F**). Together, lipidomic analysis suggests that despite morphological similarities, LCs and adipocytes rely on distinct lipid vacuole biogenesis, maintenance, and/or utilization pathways.

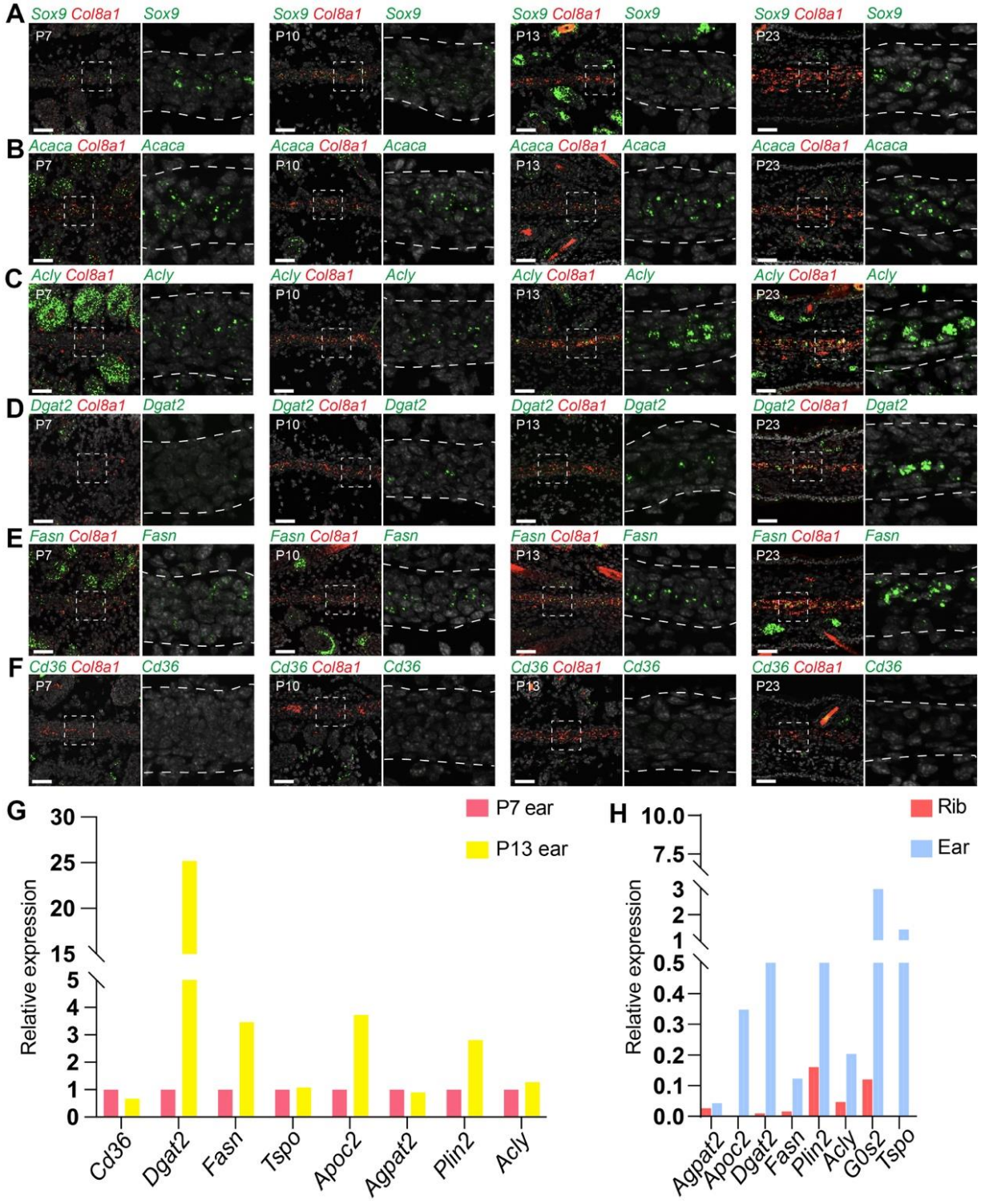
A
Sox9 Col8a1
Sox9
P7
P10
P13
P23
B
Acaca Col8a1
Acaca
C
Acly Col8a1
Acly
D
Dgat2 Col8a1
Dgat2
E
Fasn Col8a1
Fasn
F
Cd36 Col8a1
Cd36
G
P7 ear
P13 ear
Relative expression
30
25
20
15
5
4
3
2
1
0
Cd36
Dgat2
Fasn
Tspo
Apoc2
Agpat2
Plin2
Acly
H
Rib
Ear
Relative expression
10.0
7.5
3
2
1
0.5
0.4
0.3
0.2
0.1
0.0
Agpat2
Apoc2
Dgat2
Fasn
Plin2
Acly
G0s2
Tspo

Fig. S8: Validation of selected differentially expressed genes by hybridization chain reaction and qRT-PCR. (A-F) Hybridization chain reaction (RNAscope) assays show gene co-expression in developing mouse ear pinna. Co-expression of *Col8a1* (red) and *Sox9* **(A)**, *Acaca* **(B)**, *Acly* **(C)**, *Dgat2* **(D)**, *Fasn* **(E)**, and *Cd36* **(F)** was examined in P7 (leftmost column), P10 (middle left), P13 (middle right), and P23 (rightmost column) mouse ear pinna. Dashed boxes on the left-side images demarcate the magnified view on the right side, displaying the green channel only. Dashed lines on the right-side images demarcate the lipocartilage. **(G-H)** Relative expression of selected genes in different cartilages. Relative expression of genes involved in lipid metabolism and uptake between P7 and P13 microdissected ear cartilage **(G).** Relative expression of genes involved in lipid metabolism and uptake in rib cartilage and ear lipocartilage compared to white adipose tissue in one-month-old mice **(H)**. Data in **(G-H)** is generated by qRT-PCR. Abbreviations: Rib, rib cartilage; Ear, ear lipocartilage. Scale bars: (A-F), 50 μm.

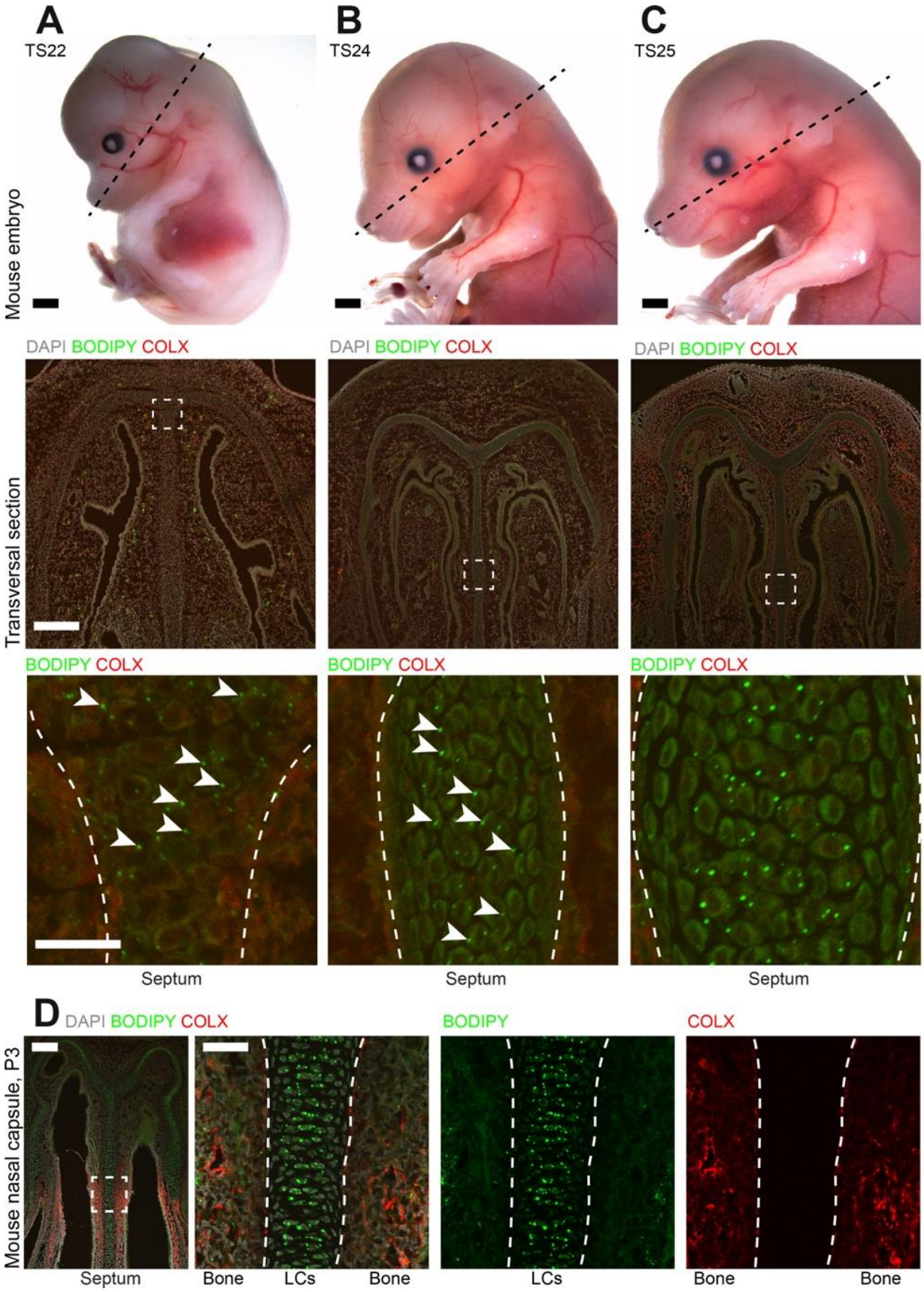
A
TS22
B
TS24
C
TS25
Mouse embryo
DAPI BODIPY COLX
DAPI BODIPY COLX
DAPI BODIPY COLX
Transversal section
BODIPY COLX
BODIPY COLX
BODIPY COLX
Septum
Septum
Septum
D
DAPI BODIPY COLX
BODIPY
COLX
Mouse nasal capsule, P3
Septum
Bone
LCs
Bone
LCs
Bone
Bone

Fig. S9: Immunostaining analysis on embryonic mouse chondrocranium and perinatal skull. (**A**) At stage TS22 (top panel), $BODIPY^+$ vacuoles (green) appear in the distal nasal septum (middle and bottom panels, arrowheads). (**B**) By TS24 (top panel), $BODIPY^+$ vacuoles appear along the proximal septum (middle and bottom panels, arrowheads). (**C**) By TS25, $BODIPY^+$ vacuoles are evident and more broadly distributed along the septum (middle and bottom panels). At this stage, collagen COLX expression (red) is confined to adjacent mesenchyme of the nasal capsule, that will eventually ossify. (**D**) Transversal section of the mouse nasal capsule at P3, stained with BODIPY for lipids (green) and co-stained with COLX antisera (red) is shown on the extreme left. The three panels on the right show a magnified view of the inset in (**A**) with annotations. $BODIPY^+$ nasal septum lipocartilage is non-overlapping and sharply demarcated from $COLX^+$ ossifying septum around it. Scale bars: (A, B, C, top), 1 mm; (A, B, C, middle), 200 µm; (A, B, C, bottom), 25 µm; (D, left), 100 µm; (D, second panel), 50µm.

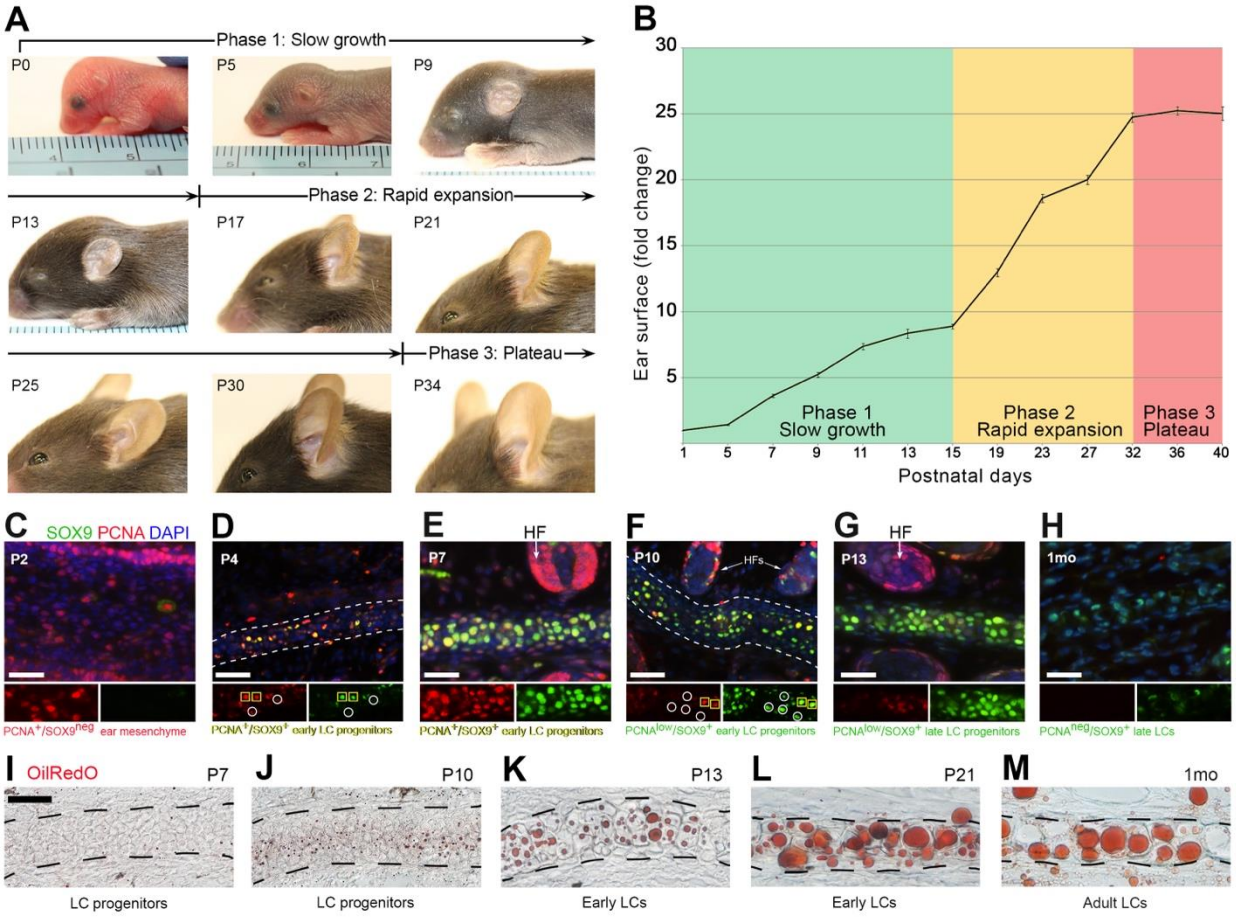

Fig. S10: Design and methodology of RNA-sequencing experiments on ear lipochondrocytes. (**A-B**) Phases of ear pinna growth in mice. (**A**) Ear pinna in mice undergoes significant size and shape changes during the first postnatal month. Representative images are shown to scale and are marked with postnatal days. (**B**) Quantification of ear surface measurements reveals three phases of ear pinna grows: Phase 1 of slow growth between days P1 and P15, when ears enlarge by approximately nine times (green); Phase 2 of rapid expansion between days P15 and P32 (yellow); and plateau Phase 3 (orange), when ears stop further expansion and become approximately 25 times larger than P1 ears. (**C-H**) Expression patterns of SOX9 and PCNA in the developing ear lipocartilage. Immunostaining for SOX9 (green) and PCNA (red) in P2 (**C**), P4 (**D**), P7 (**E**), P10 (**F**), P13 (**G**) and one month ear lipocartilage (**H**). For all time points, co-localization of markers is shown on the top panels. Bottom panels show PCNA and SOX9 expression within the same selected region but as separate channels. Single-positive cells are marked with white circles and double-positive cells with yellow squares. Double-positive cells are present in ear lipocartilage between P4 and P13. Ear lipocartilage is marked with dashed lines. (**I-M**) Lipid vacuole formation in differentiating lipocartilage by OilRedO staining. OilRedO staining in P7 (**I**), P10 (**J**), P13 (**K**), P21 (**L**), and one month (**M**) ear lipocartilage (dashed lines) shows evidence for lipid accumulation starting at around P10. HFs, hair follicles; LCs, lipochondrocytes. Scale bars: (C-M), 25 μm.

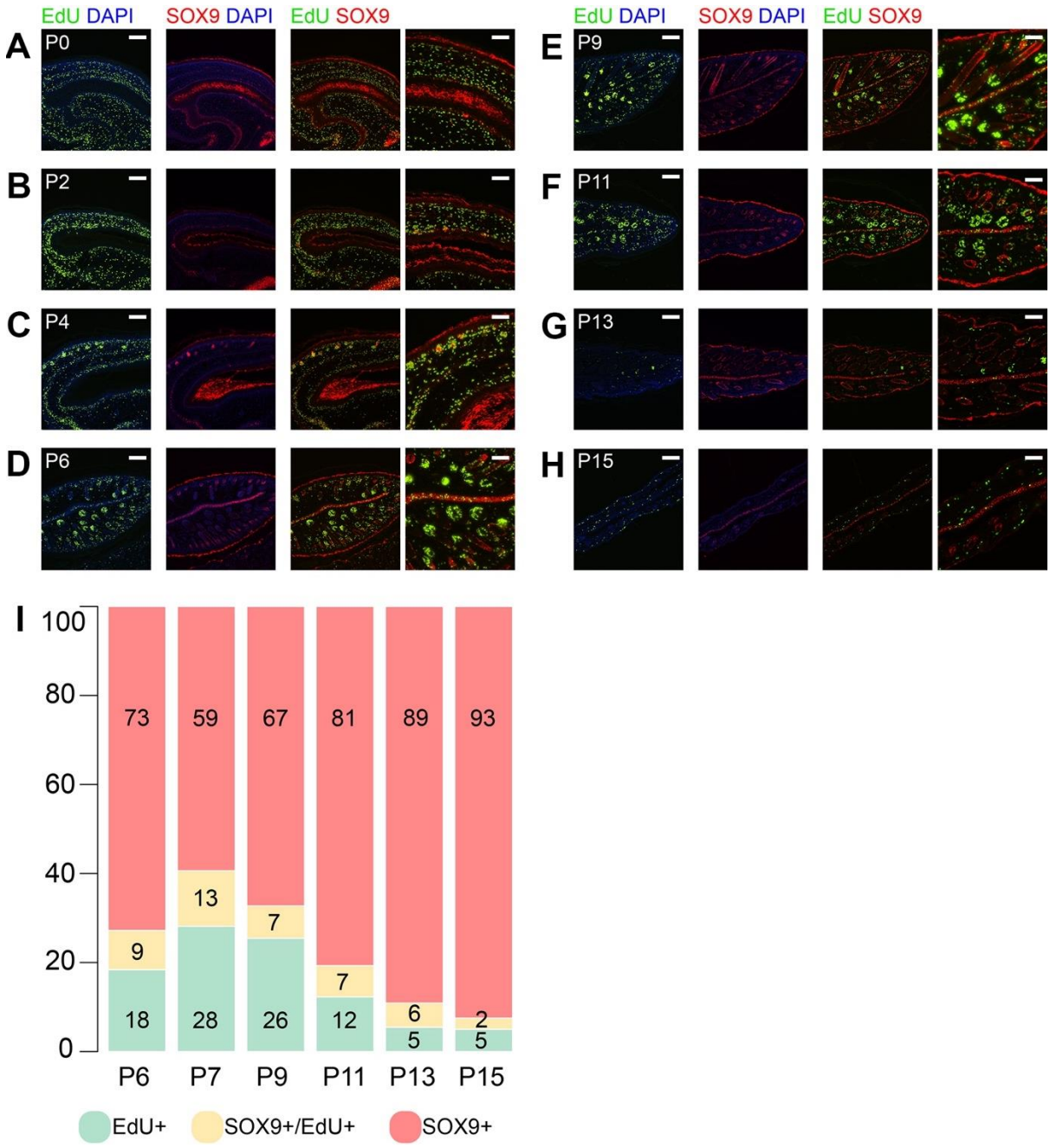

Fig. S11: Proliferative cell dynamics in relation to chondrogenic cell fate commitment in developing mouse ear lipocartilage. (**A-H**) Four hour-long EdU pulse-chase (green) and SOX9 immunolabeling (red) results are show in P0 (**A**), P2 (**B**), P4 (**C**), P6 (**D**), P9 (**E**), P11 (**F**), P13 (**G**), and P15 (**H**) ear pinnae. (**I**) Quantified results for (**A-H**) shown as a percentage plot, displaying the relative proportion of $SOX9^{neg}/EdU^{+}$ (green), $SOX9^{+}/EdU^{+}$ (yellow), and $SOX9^{+}/EdU^{neg}$ (red) cells within ear lipocartilage at specified timepoints. Labels under each stack correspond to their respective timepoint. Numbers inside each bar indicate proportion rounded to the nearest whole number. Scale bars: (A-H, left panels), 100 μm; (A-H, rightmost panels), 50 100 μm.

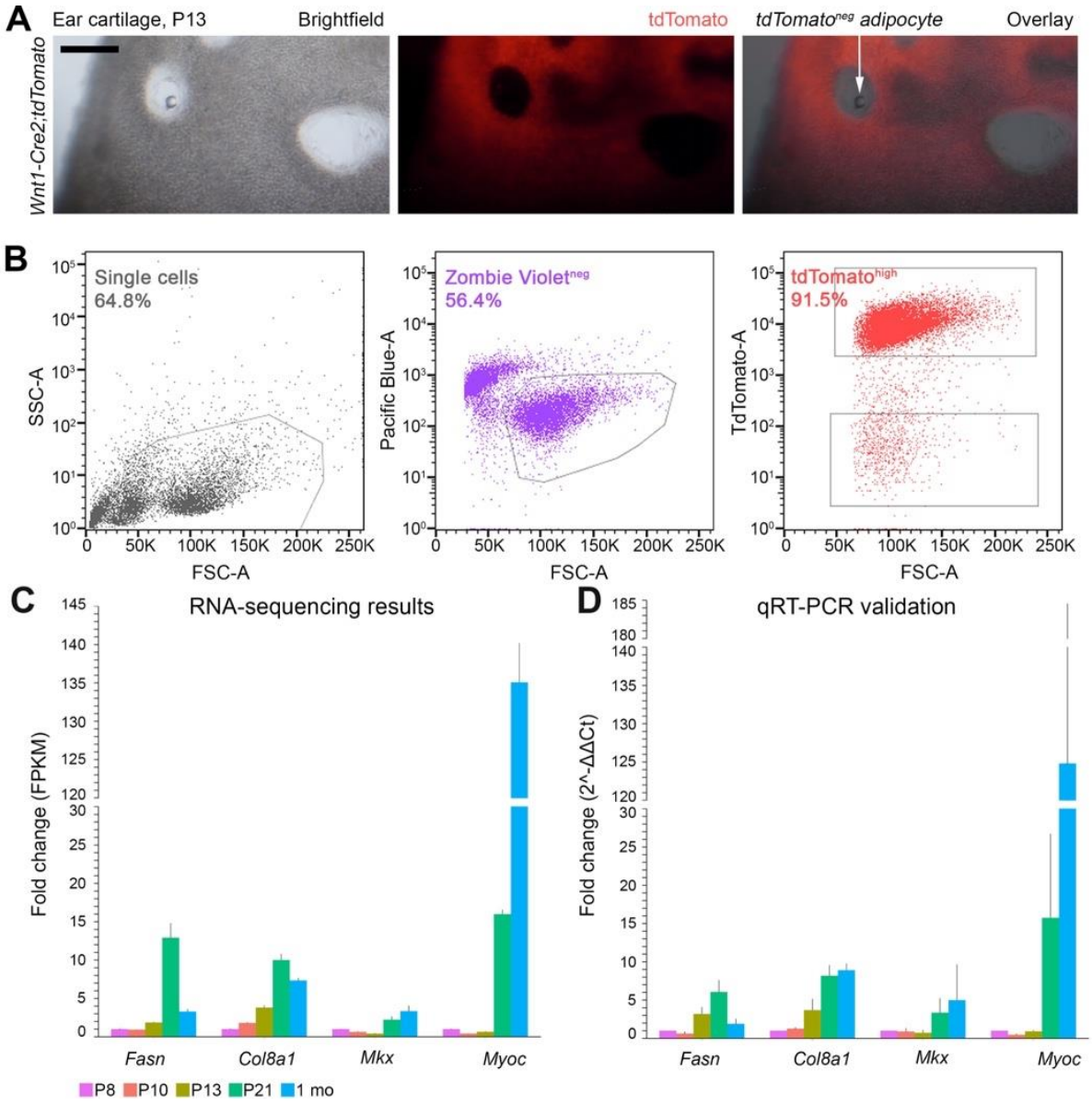

Fig. S12: Isolation and analysis of mouse ear lipochondrocytes. (**A-B**) Cell sorting strategy for isolating early lipochondrocytes. (**A**) Wholemount view of microdissected ear lipocartilage from a P13 *Wnt1-Cre2;tdTomato* mouse. Brightfield (left), tdTomato expression (center) and overlay (right) images are shown. A large portion of the ear lipocartilage is tdTomato^{+}. Adipocytes within ear fenestrae are tdTomato^{neg} (arrow on the right). (**B**) Gating strategy for sorting tdTomato^{high} viable (Zombie Violet^{neg}) early lipochondrocytes from P13 *Wnt1-Cre2;tdTomato* ear lipocartilage. (**C-D**) Verification of relative expression dynamics of differentially expressed genes by qRT-PCR. (**C**) Fold change of FPKM values of four differentially expressed genes, *Fasn, Col8a1, Mkx* and *Myoc*, during lipochondrocyte development compared to day P8. (**D**) Relative expression of the same four genes during lipochondrocyte development by qRT-PCR. The expression dynamics revealed in our RNA-seq experiments closely match those seen by qRT-PCR. Scale bars: (A), 500 μm.

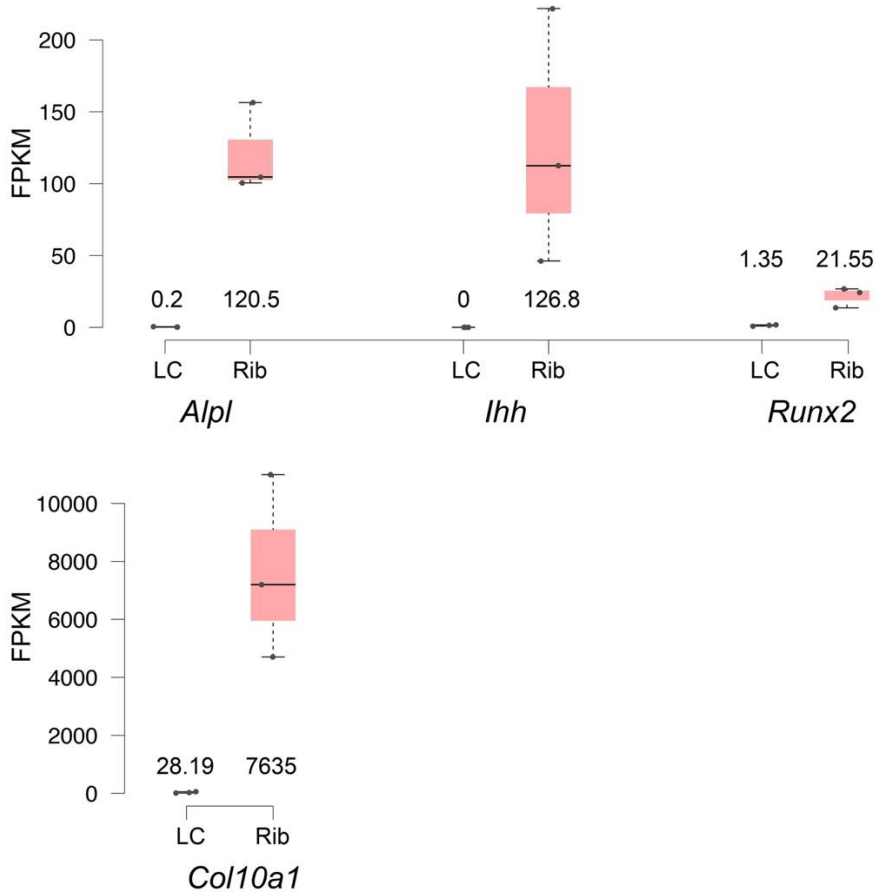

Fig. S13: Gene expression for selected cartilage hypertrophy genes. Results are based on bulk RNA-seq data generated on one-month-old mouse ear lipochondrocytes *vs.* P0 rib chondrocytes. Values accompanying boxplots indicate mean FPKM across replicates. For each gene, the lower and upper bounds of the box mark the lower and upper quartiles, respectively, while the thicker band within the box demarcates the median. Whiskers demarcate data extremes. Genes are marked below each plot, and their expression values (in FPKM) are shown along the Y-axis.

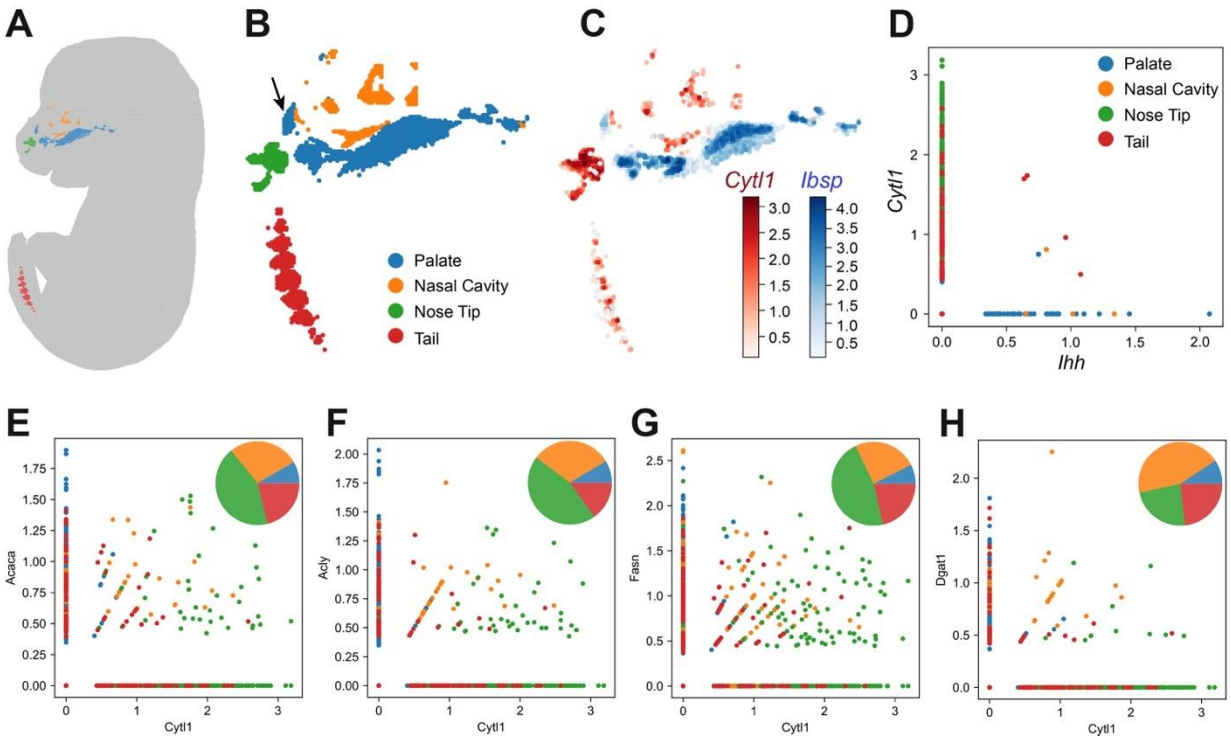

Fig. S14: Spatial transcriptomics analysis of craniofacial and caudal skeletal elements in E16.5 mouse embryo. (**A**) Stereo-seq sample of the E16.5 mouse embryo (sagittal section; entire embryo is marked grey), showing original spatial location of selected, color-coded clusters. (**B**) Digitally magnified view of selected color-coded skeletal clusters from (**A**), and their annotations. Note that *Tail* cluster was digitally moved close to facial clusters. (**C**) Spatial expression pattern of chondrogenic *Cytl1* (red) and osteogenic *Ibsp* (blue) in spatial clusters from (**B**), revealing their nearly mutually-exclusive expression. (**D**) Co-expression analysis of chondrogenic *Cytl1* and osteogenic *Ihh*, revealing their nearly mutually exclusive expression. Each dot on the plot marks one sequenced spot in Stereo-seq data. Dots are colored according to their cluster of origin. (**E-G**) Co-expression analysis of chondrogenic *Cytl1* and lipogenesis factors *Acaca* (**E**), *Acly* (**F**), *Fasn* (**G**), and *Dgat1* (**H**). Double-positive sequenced spots map to the center of the plot. The latter are also quantified and their proportional abundance in selected spatial clusters is shown in piechart insets. A majority of double-positive spots localize to facial lipocartilages (green and orange segments).

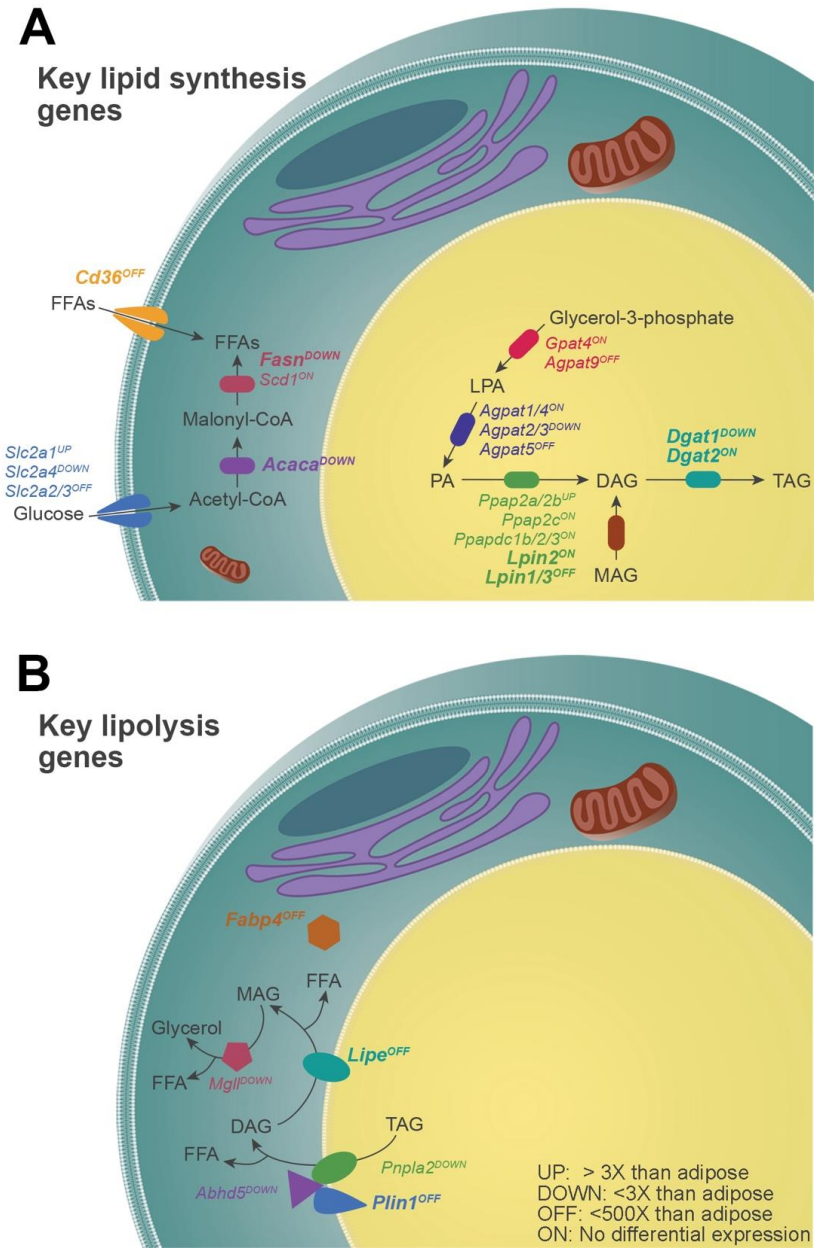

Fig. S15: Expression status of the key lipid synthesis (A) and lipolysis genes (B) in one-month-old ear lipochondrocytes. Lipochondrocyte drawings are shown with nucleus (dark teal), endoplasmic reticulum (purple), mitochondria (brown) and lipid vacuole (yellow). Genes in the drawings are positioned based on the known subcellular locations of their protein products. Genes are accompanied by the expression status: UP, DOWN, OFF and ON. Status is based on the gene's FPKM level in RNA-seq data and defined in (**B**). Also see Table S3.

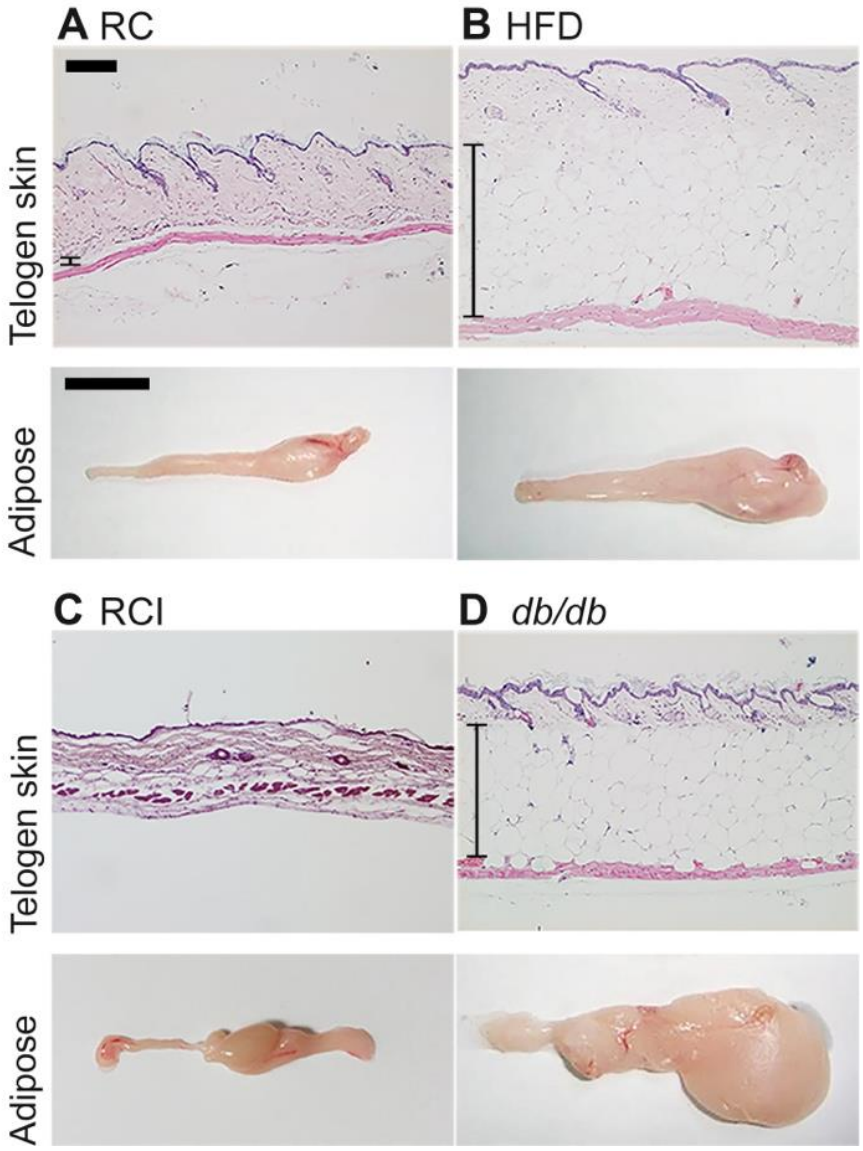

Fig. S16: Dietary modifications result in changes to mouse tissue adiposity. Relative to control fed (regular chow, RC) animals (**A**), dermal white adipose tissue (top) and perigonadal white adipose tissue (bottom) significantly increase in high fat diet mice (HFD; **B**), *db/db* mutant mice (**D**) and decrease in restricted caloric input (RCI) mice (**C**). Scale bars: (A-D, top panels), 200 μm; (A-D, bottom panels), 1 cm.

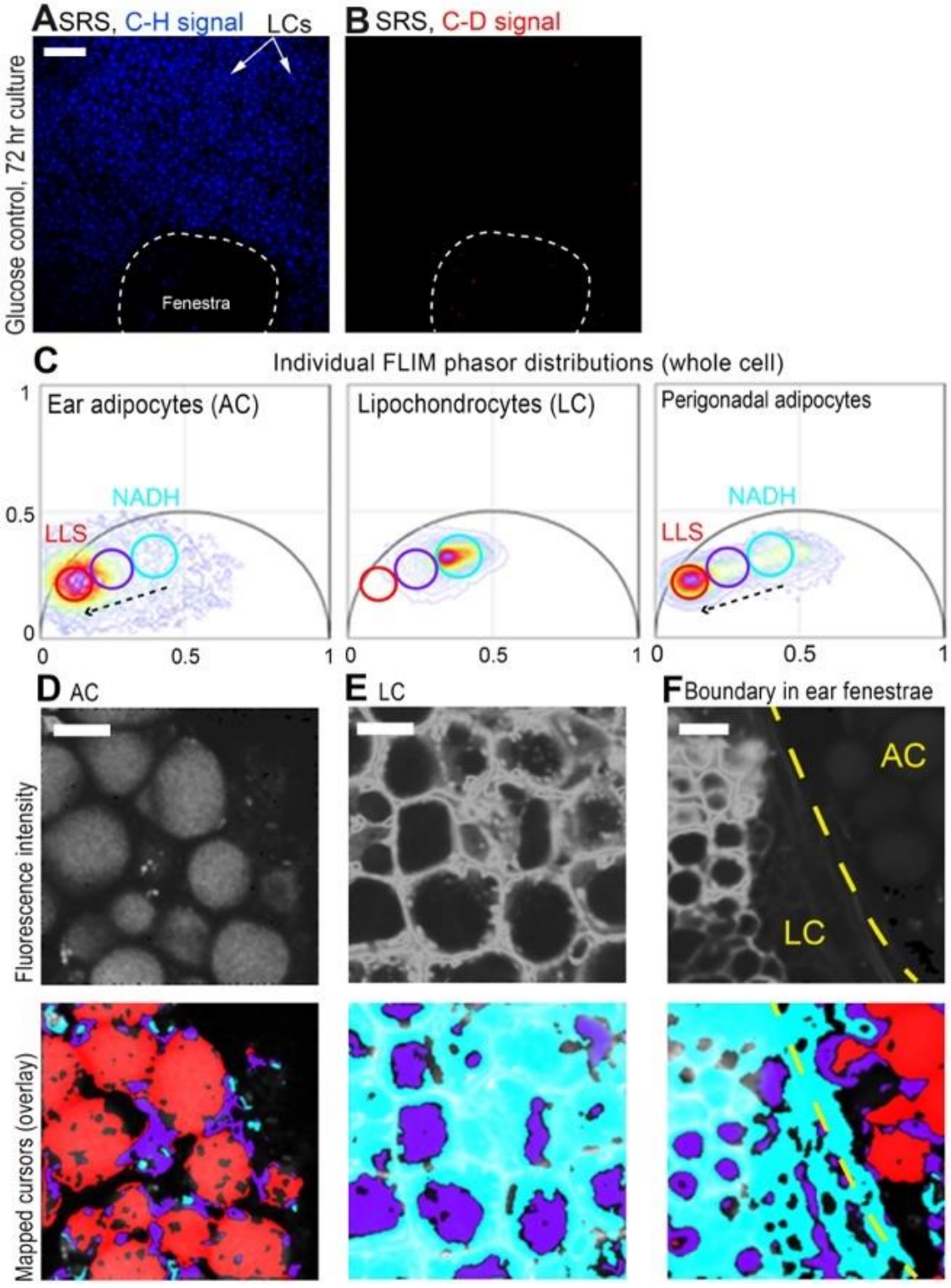
A SRS, C-H signal
LCs
B SRS, C-D signal
Glucose control, 72 hr culture
Fenestra
C
Individual FLIM phasor distributions (whole cell)
Ear adipocytes (AC)
Lipochondrocytes (LC)
Perigonadal adipocytes
NADH
LLS
1
0.5
0
0
0.5
1
D AC
E LC
F Boundary in ear fenestrae
AC
LC
Fluorescence intensity
Mapped cursors (overlay)

Fig. S17: SRS and FLIM signatures of ear lipochondrocytes. (**A-B**) SRS microscopy of cultured ear lipocartilage in the presence of normal glucose. Color-coded stimulated Raman scattering (SRS) microscopy images of P14 ear lipocartilage after 72 hours of culture in the presence of glucose control. Positive SRS signal within the C-H vibration range (~2800-3000 cm^{-1}) indicative of lipids (**A**) and SRS signal within the C-D vibration range (~2000-2400 cm^{-1}) indicative of deuterated lipids (**B**) are shown. As expected for this sample, SRS signal within the C-D vibration range is negative. Dashed lines outline ear fenestra. (**C**) Individual fluorescence lifetime imaging microscopy (FLIM) phasor plots on freshly-isolated ear adipocytes (AC, left) and ear lipochondrocytes (LC, center) following tissue excitation at 740 nm wavelength. Data from perigonadal white adipose tissue is shown on the right panel. Key endogenously fluorescent molecular species, NADH and long lifetime species (LLS), are marked and color-coded blue and red, respectively. Adipocytes, but not lipochondrocytes display strong LLS signature. (**D-F**) Mapped cursor overlays of FLIM data onto adipocytes (**D**), lipochondrocytes (**E**), and boundary of ear lipocartilage fenestrae (**F**). Top panels show endogenous fluorescence intensity and bottom panels show cursor overlays with NADH (blue) and LLSs (red), and the vector path between them (purple). LLSs colocalize to adipocytes. Scale bars: (E), 10 μm; (D, F), 20 μm; (A), 50 μm.

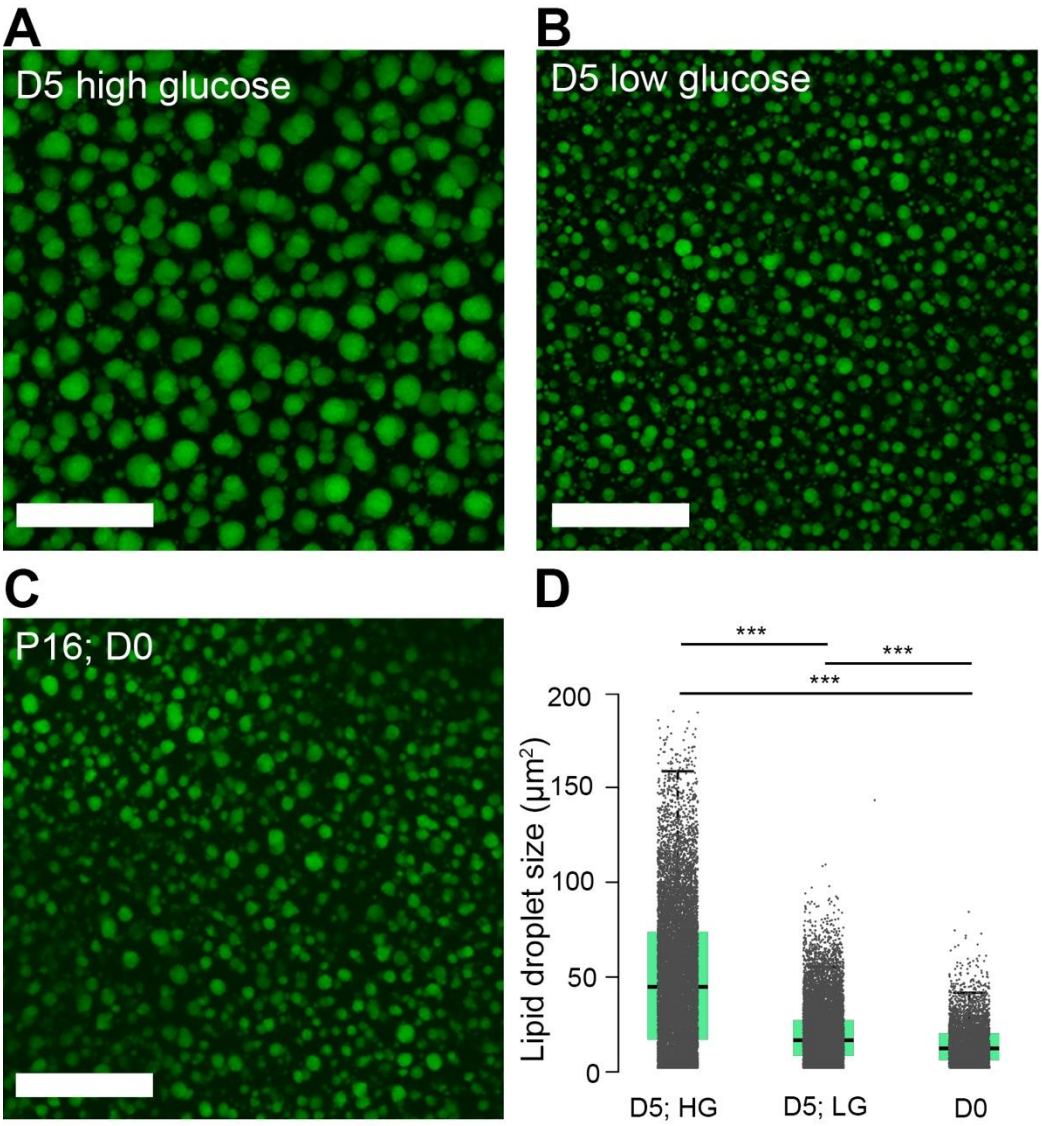

Fig. S18: Mouse ear lipocartilage differentiation in organotypic culture under different glucose conditions. (**A-C**) Representative images of BODIPY-stained lipid droplets (green) in ear lipocartilage after five days of culture under high glucose (**A**) or low glucose (**B**) conditions following micro-dissection at P16 (considered as day 0; D0) (**C**). (**D**) Quantification of lipid droplet area (in μm^2) in ear lipocartilage samples shown in (**A-C**) reveals significantly larger lipid droplets forming under high glucose condition (D5; HG) relative to low glucose (D5; LG) group. The lower and upper bounds of the box mark the lower and upper quartiles, respectively, while the thicker band within the box demarcates the median. Whiskers demarcate data extremes. On BODIPY staining after 5 days, cultured lipocartilages show significantly larger lipid droplets relative to culture day 0 (one-way ANOVA, $p<0.0001$). Lipocartilages cultured under high glucose (n=4) also show significantly larger lipid droplets relative low glucose-exposed lipocartilages (n=4) (one-way ANOVA, $p<0.0001$) Scale bars: (A-C), 50 µm.

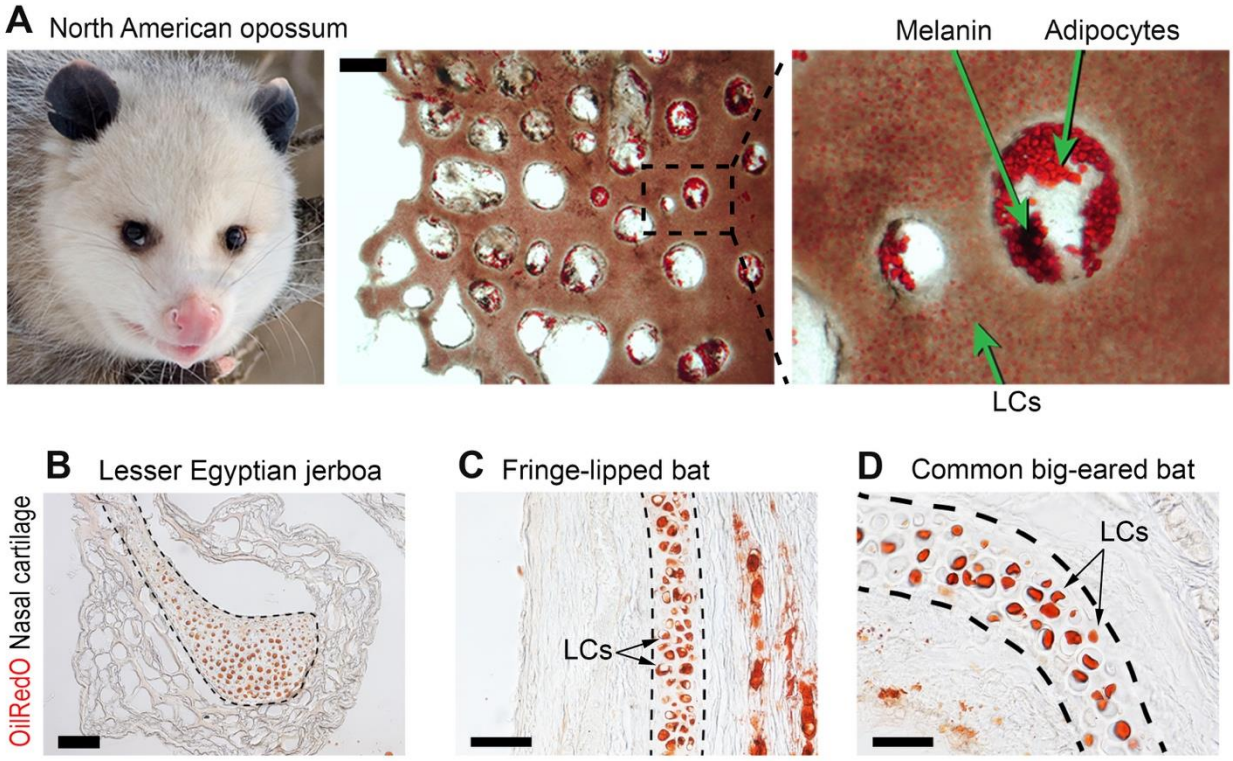

Fig. S19: Examples of ear and nasal lipochondrocytes in mammals. (**A**) Representative example of ear lipocartilage in North American opossum (*Didelphis virginiana,* marsupial). (**B-D**) Representative examples of nasal lipocartilages in Lesser Egyptian jerboa (*Jaculus jaculus,* order Rodentia) (**B**), Fringe-lipped bat (*Trachops cirrhosus,* order Chiroptera) (**C**) and Common big-eared bat (*Micronycteris microtis,* order Chiroptera) (**D**). All tissue samples were stained for lipid with OilRedO (red). LCs, lipochondrocytes. Scale bars: (B), 100 μm; (C, D), 200 μm; (A), 2 mm.

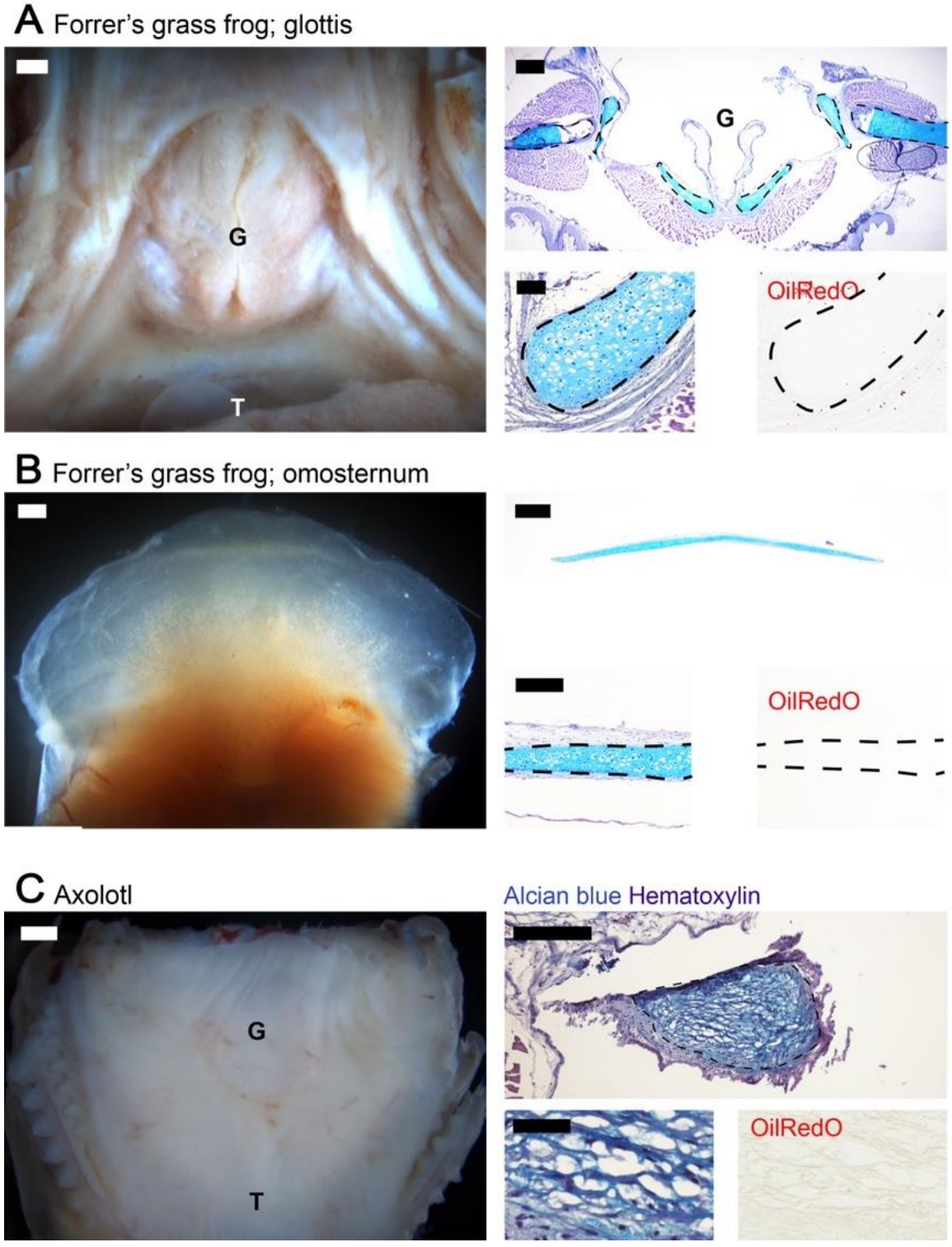
A Forrer's grass frog; glottis
G
T
G
OilRedO
B Forrer's grass frog; omosternum
OilRedO
C Axolotl
G
T
Alcian blue Hematoxylin
OilRedO

Fig. S20: Analysis of selected amphibian cartilages. (**A**) Left panel shows gross anatomy of the glottis from adult Forrer's grass frog in rostral view. Right panel (upper half) shows a cross section of the larynx stained for cartilage with alcian blue and hematoxylin (rostral side is up). Right panel (lower left quadrant) shows magnified view of alcian blue/hematoxylin-stained cartilage. Right panel (lower right quadrant) shows OilRedO staining (negative) of the same cartilage. (**B**) Left panel shows gross anatomy of the omosternum from adult Forrer's grass frog. Right panel (upper half) shows a cross section of the larynx stained for cartilage with alcian blue and hematoxylin. Right panel (lower left quadrant) shows magnified view of alcian blue/hematoxylin-stained cartilage. Right panel (lower right quadrant) shows OilRedO staining (negative) of the same cartilage. (**C**) Left panel shows gross anatomy of the mandible from Axolotl in dorsal view. Right panel (upper half) shows a cross section of the larynx stained for cartilage with alcian blue and hematoxylin. Right panel (lower left quadrant) shows magnified view of alcian blue/hematoxylin-stained cartilage. Right panel (lower right quadrant) shows OilRedO staining (negative) of the same cartilage. G, glottis; T, tongue. Scale bars: (A, left and top right), 1 mm; (A, bottom right), 100 µm; (B, left and top right), 1 mm; (B, bottom right), 250 µm; (C, left), 1 mm; (C, top right), 500 µm; (C, bottom right), 100 µm.

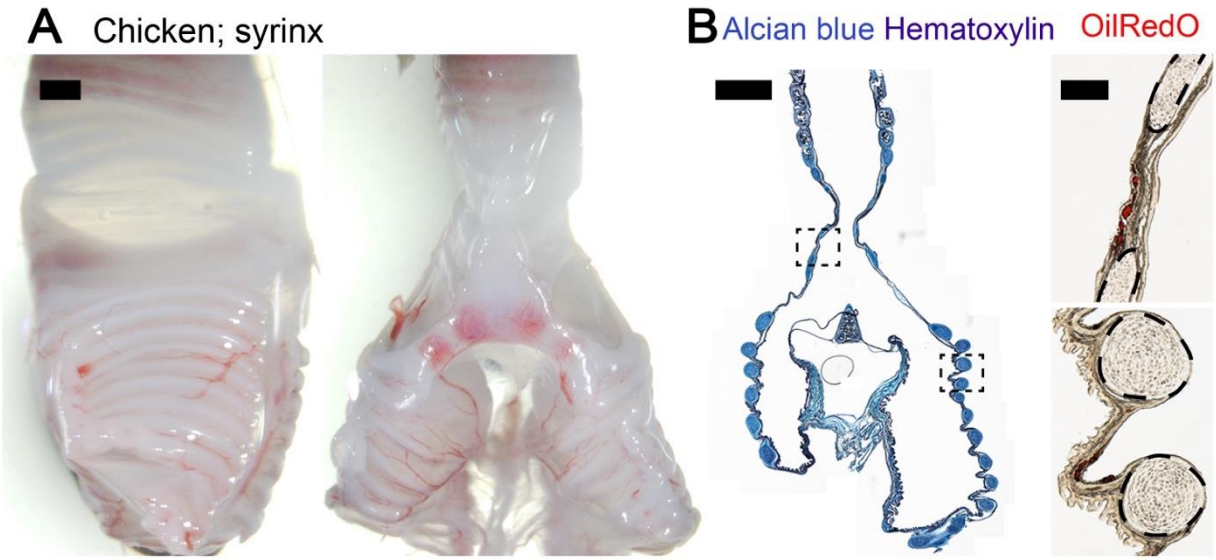

Fig. S21: Analysis of chicken syrinx cartilage. (**A**) Gross anatomy of the syrinx from adult chicken, with trachea on the top and bronchi at the bottom. Lateral view is shown on the left, ventral view is shown on the right. (**B**) Left panel shows a cross section of the proximal trachea and bronchi stained for cartilage with alcian blue and hematoxylin. Right panel shows OilRedO staining (negative) of selected cartilages. Scale bars: (A), 1 mm; (B, left), 2 mm, (B, right), 250 µm.

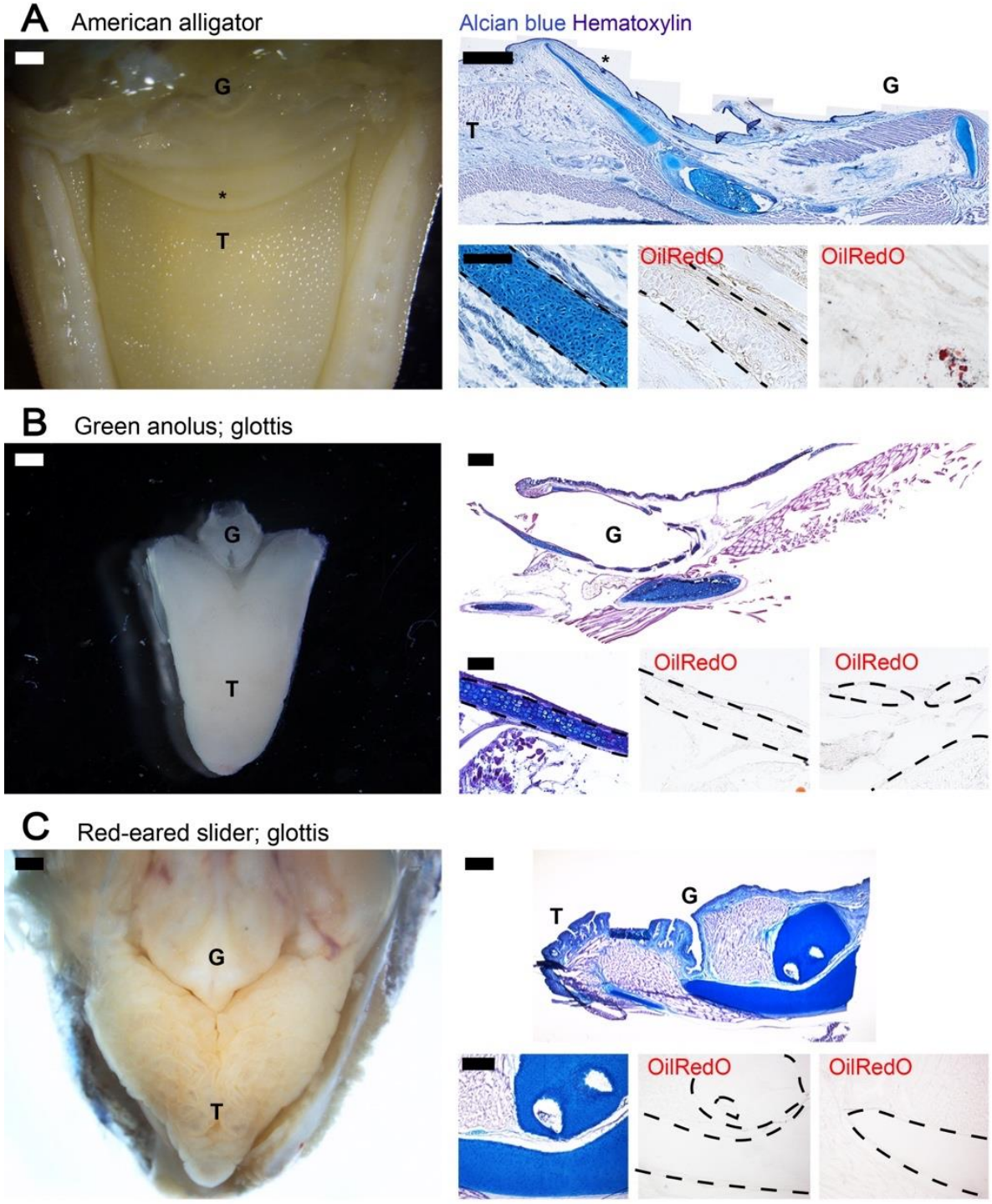
A American alligator
Alcian blue Hematoxylin
G
*
T
OilRedO
OilRedO
B Green anolus; glottis
G
T
OilRedO
OilRedO
C Red-eared slider; glottis
G
T
OilRedO
OilRedO

Fig. S22: Analysis of selected reptilian cartilages. (**A**) Left panel shows gross anatomy of the mandible from American alligator hatchling in dorsal view. Right panel (upper half) shows a cross section of the larynx stained for cartilage with alcian blue and hematoxylin. Right panel (lower left) shows magnified view of alcian blue/hematoxylin-stained cartilage. Right panels (lower central and right) show OilRedO staining (negative result) of the same cartilage. (**B**) Left panel shows gross anatomy of the dorsal aspect of the tongue and glottis from an adult Green anole lizard. Right panel (upper half) shows a cross section of the larynx stained for cartilage with alcian blue and hematoxylin. Right panel (lower left) shows magnified view of alcian blue/hematoxylin-stained cartilage. Right panels (lower central and right) show OilRedO staining (negative result) of the same cartilage. G, glottis; T, tongue. (**C**) Left panel shows gross anatomy of the mandible from adult Red-eared slider turtle. Right panel (upper half) shows a cross section of the larynx stained for cartilage with alcian blue and hematoxylin (rostral side is up). Right panel (lower left) shows magnified view of alcian blue/hematoxylin-stained cartilage. Right panels (lower central and right) show OilRedO staining (negative result) of the same cartilage. G, glottis; *, palatal valve; T, tongue. Scale bars: (A, left and top right), 1 mm; (A, bottom right), 100 µm; (B, left), 1 mm; (B, top right), 300 µm; (B, bottom right), 100 µm; (C, left and top right), 1 mm; (C, bottom right), 500 µm.

Captions

Table S1: Comparative lipidomic analysis between one-month-old ear lipocartilage and inguinal white adipose tissue.

Table S2: Comparative proteomic analysis (mass spectrometry) between one-month-old ear lipocartilage and inguinal white adipose tissue.

Table S3: Comparative transcriptomic analysis between one-month-old ear lipochondrocytes, inguinal white adipocytes and hyaline rib cartilage chondrocytes.

Table S4: Gene Ontology analysis on differentially expressed genes between one-month-old ear lipochondrocytes, inguinal white adipocytes and hyaline rib cartilage chondrocytes.

Table S5: Time course transcriptomic analysis on developing ear lipochondrocytes.

Table S6: Select genes within cell cycle, lipogenesis, transcription, signaling and extracellular matrix categories differentially expressed during ear lipochondrocyte development.

Table S7: Gene Ontology analysis on differentially expressed genes across time course of ear lipochondrocyte development.

Table S8: Comparative transcriptomic analysis between hESC-derived cartilage pellets at differentiation days 21, 30, and 45, including detected expression (TPM) and temporally-relevant clusters P1-P5.

Table S9: Phylogenetic information on analyzed craniofacial tissue samples.

Table S10: Primer sequence information for genotyping and gene expression experiments.

Movie S1: Three-dimensional rendering of BODIPY-stained microdissected ear lipocartilage from one-month-old wild type mouse.